pH drives electron density fluctuations that enhance electric field-induced liquid flow

S. Pullanchery[1*], S. Kulik[1*], T. Schönfeldová[1], G. Cassone[4], A. Hassanali[5#], S. Roke[1.2.3#]

[1]Laboratory for fundamental BioPhotonics, Institute of Bioengineering (IBI), School of Engineering (STI), École Polytechnique Fédérale de Lausanne (EPFL); CH-1015, Lausanne, Switzerland.
[2]Institute of Materials Science and Engineering (IMX), School of Engineering (STI), École Polytechnique Fédérale de Lausanne (EPFL); CH-1015, Lausanne, Switzerland.
[3]Lausanne Centre for Ultrafast Science, École Polytechnique Fédérale de Lausanne (EPFL); CH-1015, Lausanne, Switzerland.
[4]Institute for Physical-Chemical Processes, Italian National Research Council (IPCF-CNR); Messina, Italy.
[5]International Centre for Theoretical Physics; Trieste, Italy.
*both authors contributed equally
[#]_ahassana@ictp.it_; _sylvie.roke@epfl.ch_

ABSTRACT

Liquid flow along a charged interface is commonly described by a classical continuum theory, which assumes ionic groups as responsible, uniformly distributed point charge carriers. Within this framework, electric field-induced flow (electro-osmosis or -phoresis) arises from charged ionic groups at the surface that interact with an external field. Changing bulk pH doubles the electrophoresis and osmosis by changing the number of surface charges. Here, we challenge this idea, combining measurements of hydrophobic nanodroplet velocity in water under an external field, all-optical surface charge density, and surface molecular structure measurements with quantum level computations. We show that classical continuum theory fails under the general case that the pH of the solution is varied and that the resulting increase in mobility originates from charge density fluctuations. The force that propels the droplets originates from gradients in the fluctuating electron polarizability that interact with the external electric field. Basic solutions display hydroxide-induced and electric field-enhanced charge asymmetry. This doubles the solutions' charge conductivity, manifesting as a change in the solutions' polarizability. The electromagnetic energy gradient responsible for the propelling force is proportional to the solutions' polarizability, which leads to the remarkable influence of bulk pH on electrophoresis (and -osmosis). This general mechanism deeply impacts a plethora of processes in biology, chemistry, and nanotechnology and provides a unified explanation of how pH influences hydrodynamics.

Introduction

Liquid flow of an electrolyte solution in contact with a charged surface is commonly modeled using the Navier-Stokes equations that combine the continuity equation (conservation of mass), energy and momentum conservation, and the Poisson-Boltzmann equation to describe charge distribution[1]. This classical continuum approach works well to understand liquid flow in many situations, even down to the nanoscale[2-5]. However, this description relies on assumptions that are not generally valid: A structureless dielectric continuum, strong water-surface interactions to avoid liquid-surface slip, ions / charged groups as the only charge carriers, represented by point charges and giving rise to uniform charge distributions[1]. Therefore, theoretical considerations aimed at investigating the use of a continuum vs atomistic description[6,7], the inclusion of dipolar/quadrupolar interface contributions of oriented water[8], surface friction and slip[9-13], and the inclusion of droplet deformation[14], explicit distribution of ions in the electric double layer[15], among other things, have been considered. These models describe how diverse effects impact electrophoretic phenomena. However, determining the correct representation of reality requires explicitly verifying the various model ingredients by independent measurements.

As an example of this challenge, the following well-known pH-induced phenomena can be considered: Pressure driven electro-osmosis through hexagonal boron nitride nanocapillaries[16], carbon nanotubes[17], graphene oxide membrane conductance[18], and streaming currents through MoS_2 pores[19] in aqueous solutions all display a remarkable increase in current (x 2-3) when the pH of the surrounding bulk solution is increased to mildly basic solutions (1 mM NaOH, pH 11). Hydrophobic nanoparticles, droplets, and gas bubbles of different materials all display the same pH-dependent electrophoretic mobility[20-26]: increasing the pH of the surrounding aqueous bulk phase to the same mildly basic value results in an x 2-3 increase in droplet mobility under the influence of an external electrostatic field. All the involved poorly wetted surfaces in water are negatively charged, and according to classical-continuum theory, this charge apparently more than duplicates under the influence of small changes in the bulk concentration of OH^-, increasing the current / mobility in an external electrostatic field[20,27]. Curiously, the pH-induced increase in currents[16-19]/ mobility[20-26] is identical in all of these cases, even though the substrates/systems are vastly different. It is well known that ion-interface interactions are very sensitive to the ionic species and the chemical composition of the interface, and such effects manifest themselves > 0.1 M ion strength[28]. Therefore, from a surface chemistry perspective, it is highly unlikely that dilute hydroxide bulk concentrations should lead to identical surface charging due to the surface activity of the hydroxide ions in this wide variety of systems.

Furthermore, it is well known that charge flow in basic solutions is enhanced by the Grotthuss mechanism[29] that consists of concerted hydrogen (H-)bond network correlations. These correlations facilitate migration of negative charge through transient hydrogen-bond network structures which involves proton transfer[29,30]. Correctly describing charge flow likely requires including such fundamental ingredients. Oil nanodroplets in water are a well-studied hydrophobic-water model system[20,21,31]. Their surface charge/ mobility has been attributed to the following surface ionic species: adsorbed OH^-, as it is naturally present in water[21], but also adsorbed HCO_3^- from atmospheric CO_2[32], or deprotonation of surface-active impurities from either water or oil[33,34]. However, no such ions were detected on the surface[31,35,36]. Recently, interfacial nanodroplet charge was correlated with a blue shift in the interfacial C-H stretch vibrational modes of the oil nanodroplet and a red shift in O-H stretch modes of adjacent water. This demonstrated that the negative droplet charge needs to be explained on the quantum level: Charge transfer between water and oil via improper H-bonds is responsible for surface charging[35,37]. Thus, for the general case of pH-induced electrophoresis/osmosis, it is implausible that a classical-continuum description is correct. However, to explain electric field-induced flow, mobility needs to be combined with other surface-atomistic parameters. In fact, it requires experimentally determining critical parameters, such as surface structure and potential, independently as a function of pH.

Here, we show that a classical description of electrophoretic phenomena breaks down under the very general case in which the pH of the solution is varied and that, instead, a quantum level description is needed to understand both bulk and surface behavior. We measured flow, electrostatic interface potential and molecular structure as a function of pH via three independent methods on the same hexadecane oil nanodroplet water system. We measure mobility (Fig. 1A) of the droplets when subjected to an external electrostatic field, the surface potential using an all-optical method (Second Harmonic Scattering, Fig. 1B), and the molecular surface structure independently, while exchanging the electrolyte in the aqueous bulk phase. Replacing a dilute chloride solution by a dilute hydroxide solution, we record a x 2.2 increase in droplet mobility, which is identical to the increase in charge conductivity of both bulk droplet-free aqueous solutions. However, the nanodroplets' electrostatic surface potential remains unchanged. The molecular surface structure and charge transfer of oil nanodrops and interfacial water is also independent of the type of anion present in the solution. Both datasets completely disagree with expectations from classical continuum theory. Investigating Cl^- and OH^- ions in neat water using quantum level ab-initio molecular dynamics simulations (AIMD), we find that an external electrostatic field strongly modifies the charge distribution in bulk solution, leading to an enhanced charge density in basic solution, which is also distributed preferentially along the field lines. No such effects are observed for the Cl^- solution. Simulating neopentane (C_5H_{12}) in water under an external electrostatic field, we find that the field induces

3

a measurable electronic charge separation in the solute. Droplet mobility arises from an electrostatic field-induced gradient in the electrodynamic energy that arises from a coupling between the electric field and the polarizability. This force thus originates from field-induced changes in the mobile interfacial charge distribution on the droplet, and is also reproduced by the simulation of the neopentane where a drift is observed that is consistent with the experimentally measured mobility. Hydroxide ions modify the polarizability (x 2) of the bulk solution, enhancing the anisotropy of the surface charge distribution further, resulting in a doubling of the droplet mobility. Thus, quantum mechanical charge fluctuations need to be explicitly included in the energetics / electrodynamics that underlies droplet mobility, modifying interfacial (charge transfer) and bulk (pH) responses.

Electric field-induced droplet mobility

When oil nanodroplets or other small particles in water are subjected to an electrostatic field (**E**), the droplets move toward the anode with a speed v, and a mobility $\mu = \frac{v}{E}$ (Fig. 1A). Classically, the mobility is converted to a ζ-potential, commonly interpreted as the electrostatic potential close to the surface due to the presence of ions/charged groups, via

$$\mu = \frac{\epsilon_0 \epsilon \zeta f(\kappa R)}{\eta} \tag{1}$$

where ϵ_0 is the vacuum permittivity, ϵ is the relative permittivity, η is the viscosity of the medium and $f(\kappa R)$ is the Henry's function (Eq. S1) that has a value between 2/3 and 1 depending on the radius R of the droplet and the Debye screening parameter κ[1]. $1/\kappa$ represents the 1/e decay length of the electrostatic potential, which depends on the ionic strength of the solution. We prepared hexadecane nanodroplets in water by ultrasonication (SI, S1, Fig. S1). Fig. 1C shows the average ζ-potential values of 0.05 vol% hexadecane droplets in the presence of 1 mM NaCl (pH neutral, average radius 105 nm) and 1 mM NaOH (pH 11, average radius 113 nm). Upon replacing Cl- with OH- ions, the mobility / ζ-potential magnitude increases by a factor of 2.2. This dramatic pH-dependence is in excellent agreement with previous experiments (e.g., Ref.[25] from ~-51 mV at pH=6 to ~-100 mV at pH = 9, with ionic strength fixed at 1 mM).
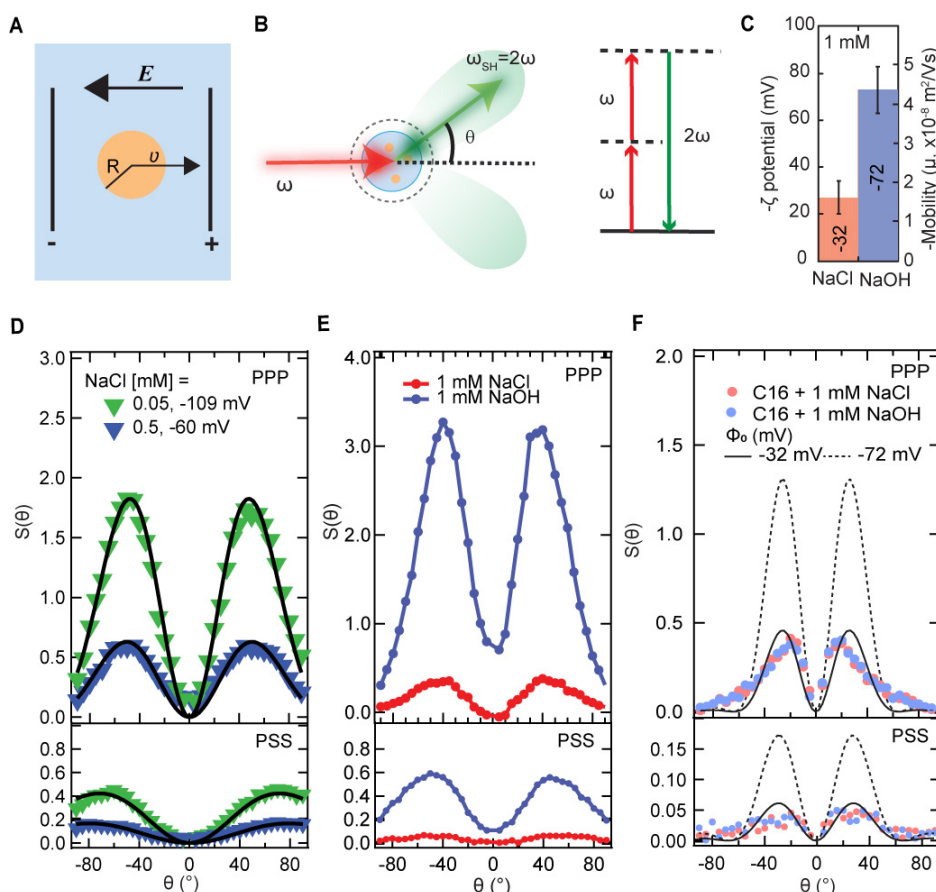
4

Figure 1. Mobility is pH-dependent but surface charge is not. (A) Illustration of an electrokinetic mobility (μ) measurement. A droplet with radius R that has an interfacial charge is moved by an electrostatic field (E), resulting in a velocity $v = \mu E$. (B) Angle-resolved second harmonic scattering. Near-IR fs laser pulses interact with droplet interfaces in a non-resonant SH scattering process. The SH photons are detected at different scattering angles. Inset: energy level scheme. (C) The ζ-potential values of 0.05 vol% ~105 nm radius hexadecane droplets in 1 mM NaCl (red) and 1 mM NaOH (blue) solutions, computed using Eqs. 1 and S1. The error bar denotes the standard deviation of 3 measurements performed on each of 5 different samples. The average mobility values are μ = -2.2 · 10^{-8} m²/Vs (NaCl) and μ = -4.8 · 10^{-8} m²/Vs (NaOH), respectively. (D) Angle resolved SHS patterns, measured in both PPP (top) and PSS (bottom) polarization combinations, obtained from 0.2 vol%, 120 nm diameter 1,2-dioleoyl-sn-glycero-3-phospho-L-serine (DOPS) liposomes in aqueous solution, containing 0.05 mM (green data) and 0.5 mM (blue data) NaCl. The surface potentials of the liposomes are -109 mV (green data) and -60 mV (blue data) respectively. PPP refers to all beams polarized in the horizontal scattering plane, and PSS refers to the SH beam polarized in the scattering plane, and the fundamental beam polarized perpendicular to it. (E) Angle resolved SHS patterns, measured in both PPP (top) and PSS (bottom) polarization combinations, obtained from 0.1 w.w.% 300 nm diameter silica nanoparticles in aqueous solution with 1 mM NaCl (red) and 1 mM NaOH (blue). (F) Measured SH $S(\theta)$ scattering patterns of 0.05 vol% hexadecane droplets in 1 mM NaCl (red data) and 1 mM NaOH (blue data) using PPP and PSS polarization combinations. The black lines represent calculated SH $S(\theta)$ patterns in both polarization combinations, having Φ_0=-32 mV (solid line) and Φ_0=-72 mV (dashed line), see SI section S1, Eqs. S2-S4, Tables S1-S4 for method, equations and parameters.

pH-dependent surface charge

Next, we determined the droplet surface potential (Φ_0) using an all-optical method as a function of pH, and constant ionic strength. Φ_0 is defined as the negative integral of the electrostatic field from the bulk aqueous solution up to the interfacial Gibbs dividing plane. Φ_0 is retrieved from angle-resolved second harmonic scattering (SHS) measurements. In a non-resonant SHS experiment, a pulsed femtosecond (fs) near-infrared laser beam interacts with the

5

droplets in solution (Fig. 1B). Coherent SH photons are emitted from all non-isotropic molecules that are anisotropically distributed. Since interfacial water is anisotropically distributed along the radial direction, while the bulk liquid is not, SHS has an exquisite interfacial sensitivity. Isotropically oriented molecules in bulk water display a weak but clearly visible SH emission that is not directional. We use these SH photons to calibrate the interfacial intensity, and measure the quantity $S(\theta)$. $S(\theta)$ represents the coherent interfacial SH intensity relative to the incoherent response of bulk water (Eq. S2)[38]. $S(\theta)$ provides a calibrated intensity that is (1) comparable to any nanoparticle surface response, and (2) allows for calculating the surface potential (Φ_0) and interfacial water ordering (quantified by the second-order susceptibility, $\chi_{s,2}^{(2)}$). By considering the combined interactions of the optical fields and the intrinsic interfacial electrostatic field with the optical properties of water, it is possible to theoretically derive equations for $S(\theta)$ that connect Φ_0 and $\chi_{s,2}^{(2)}$[38,39]. The equations are given in the SI (S1, Eqs. S3-S4). Besides varying the scattering angle, it is also possible to change the polarization state of the optical beams. Of the four possible polarization combinations that lead to SH emission from non-chiral interfaces, two independent polarization combinations (PPP and PSS) remain. Thus, having 2 sets of scattering patterns with 2 unknowns, $\chi_{s,2}^{(2)}$ and Φ_0, can be determined for a given droplet size distribution, without making any modeling assumptions on the surface structure / surface electrostatics. For particles < 300 nm in radius, this method is exceptionally sensitive to changes in either the surface chemical structure (via $\chi_{s,2}^{(2)}$) or the electric double layer (via Φ_0), especially for electrolyte concentrations < 10 mM[38,40,41]. To illustrate this exquisite sensitivity, Fig. 1D shows SHS $S(\theta)$ patterns recorded from aqueous solutions of charged liposomes (obtained from the same stock solution) having Φ_0 values that differ by a factor of ~2 (changing between -60 mV and -109 mV). The SHS patterns vary drastically in shape and intensity (x 3). Fig. 1E shows SHS patterns from silica nanoparticles dispersed in 1 mM NaCl (red data) or 1 mM NaOH (blue data) solution. Both $S(\theta)$ patterns, recorded from dispersions having the same number of particles with the same size distribution, are ~10 x different in intensity. Both these examples demonstrate the unique sensitivity of the SHS experiment to surface potential (1D) and surface structure (1E). Therefore, if replacing 1 mM NaCl by 1 mM NaOH in a solution of oil droplets in water, would result indeed in a change in surface potential by a factor of ~2.3, this should be reflected in a drastic change of the SHS pattern.

Fig. 1F shows the measured SH $S(\theta)$ patterns of 100 nm radius oil droplets in 1 mM NaCl (red) and 1 mM NaOH (blue), having ζ-potential values of -28 ± 4 mV and -88 ± 11 mV, respectively. The two scattering patterns obtained in NaCl and NaOH solutions are indistinguishable. The black solid line is a computation of the SHS scattering response $S(\theta)$

with Φ_0=-32 mV, which describes the data reasonably well. Increasing the surface potential, while keeping all other parameters the same, results in the black dashed line, which is ~2.8 x higher in intensity. Clearly, the measured data does not show this trend. Thus, for oil droplets in water, the interfacial properties Φ_0 and $\chi_{s,2}^{(2)}$ are not changing when Cl⁻ is replaced by OH⁻ in the bulk aqueous phase. Increasing the pH from neutral to pH=11 at identical ionic strength does not change the surface charge density, as has historically been concluded based on the ζ-potential data of Fig. 1C.
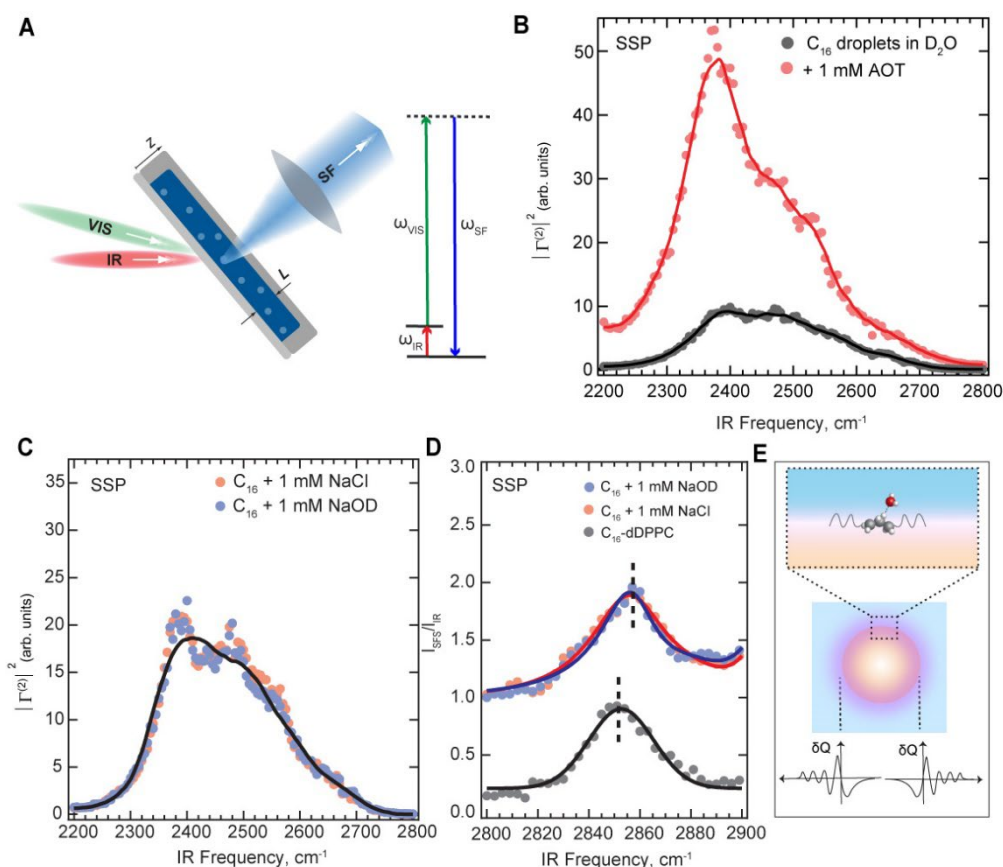

Figure 2. H-bonding network and charge transfer mechanism are pH-independent. (A) Vibrational sum frequency scattering: Simultaneous excitation using pulsed fs IR and VIS laser beams results in a simultaneous IR and Raman excitation that gives rise to scattered sum frequency (SF) photons that report on the interfacial molecular vibrational spectrum. (B) The O-D stretch spectrum of 2 vol% 100 nm radius hexadecane droplets in pure D_2O (black) and in the presence of 1 mM sodium bis(2-ethylhexyl) sulfosuccinate (AOT) surfactant, measured with the SSP polarization combination (SF and VIS beams polarized perpendicular to the scattering plane, IR beam polarized parallel to the scattering plane). (C, D) Vibrational SFS spectra of O-D stretch modes (C) and C-H stretch modes (D) of 2 vol% hexadecane droplets in D_2O at pD 7 (1 mM NaCl, red) and pD 11 (1 mM NaOD, blue) recorded using the SSP polarization combination (SF and VIS beams polarized perpendicular to the scattering plane, IR beam polarized parallel to the scattering plane). The gray curve shows C-H stretch modes of oil droplets that are not interacting with water, achieved by covering them with a dense monolayer of deuterated DPPC lipids. Solid lines represent the running average as a guide to the eye. Note that the data in Fig. 2C and 2D are not normalized. (E) Schematic illustration of charge distribution at the interface of an oil nanodroplet as a consequence of improper H-bonding / charge transfer effects.

pH-dependence of the interfacial H-bond network and charge transfer

In order to determine the interfacial H-bond and oil C-H structure as a function of pH, we used vibrational sum frequency scattering (SFS) spectroscopy. Vibrational SFS relies on the interaction of an infrared (IR) and visible (VIS) beam with the droplet dispersion (Fig. 2A). SF photons are scattered from regions where the molecules in the otherwise isotropic solutions are anisotropically arranged, i.e., they are scattered from the interface of the droplets reporting on the interfacial structure of the hexadecane and water molecules. Like SHS, SFS is exceptionally sensitive to surface chemistry. The interfacial water response, as in SHS, reports on both the surface structure (via $\chi_{s,2}^{(2)}$) and the surface potential (Φ_0) according to similar expressions that are now frequency-dependent and include a vibrational resonance. The C-H stretch region reports on the chain conformation of alkyl chains, while the O-D stretch region reports on both the surface potential (via the intensity) and the surface H-bond network structure (via the spectrum). Fig. 2B shows the effect of adding 1 mM of surface-active compound (sodium bis(2-ethylhexyl) sulfosuccinate (AOT)) to the aqueous solutions of oil nanodroplets in water for the O-D stretch region. The effect this has on the C-H stretch region is shown in Fig. S2. As with SHS, adding 1 mM leads to big changes (x 5) in SFS intensity, supplemented by changes in spectral shape. Thus, nanodroplet surface adsorption, even at bulk millimolar concentrations, results in drastic changes in vibrational SFS spectra.

Fig. 2C shows SFS $|\Gamma^{(2)}|^2$ spectra in the O-D stretch region obtained from 100 nm radius hexadecane droplets dispersed in D_2O solutions with 1 mM NaCl (pH neutral, red) and 1 mM NaOD (pH = 11, blue). The SI contains information about the sample preparation[42] and the SFS method[35,43] (SI, S1). Fig. 2D shows spectra recorded in the C-H stretch region, which reports on the interfacial oil. For the interfacial water, the SF spectra obtained at pD 7 and pD 11 consist of previously identified features[35,44]: Two broad features around 2395 cm^{-1} and 2500 cm^{-1} that correspond to H-bonded water molecules at the interface, with the latter being more weakly H-bonded compared to the former. Approximately half of the spectral broadening arises from vibrational coupling[44]. The shoulder above 2600 cm^{-1} was attributed to O-D bonds that do not form H-bonds with other water molecules, but rather participate in weak improper H-bonds with the C-H groups of the oil, as illustrated in Fig. 2E. These improper H-bonds are responsible for the transfer of a tiny amount of charge from water to oil (~0.015 e-/nm^2)[37], which generates the negative charge on the oil droplets[35], responsible for their stability (Fig. 2E). Interestingly, the spectrum recorded in the presence of 1 mM NaOD (pD 11, Fig. 2C, blue) is indistinguishable from the one recorded in the presence of the 1 mM NaCl (pD 7, Fig. 2C, red). This implies that OD$^-$ and Cl$^-$ ions have identical impacts on the interfacial H-bond network. Thus, there are no pH-induced differences in the H-bond network at the interface between oil droplets and water.

The SFS spectra of the interfacial C-H modes (Fig. 2D) show both the symmetric CH_2 (CH_2-ss) and CH_3 (CH_3-ss) stretch modes around ~2850 cm^{-1} and ~2878 cm^{-1}, respectively. Spectra are recorded for bare oil droplets in pD 7 (red data) and pD 11 (blue data) water, and compared to oil droplets that were covered with a monolayer of deuterated 1,2-dipalmytoil-sn-glycero-3-phosphocholine (d-DPPC, 0.48 nm^2/lipid[45], gray data), a zwitterionic lipid. The purpose of the lipid monolayer is to shield the oil from interacting with the water, and to simultaneously remove the interfacial charge[35]. The oil CH_2-ss modes adjacent to the deuterated lipid alkyl tails of the charge neutral droplets vibrate at lower frequencies (2851 cm^{-1}) than the CH_2-ss modes of the charged bare oil droplets that are adjacent to pH neutral water (2856 cm^{-1}). This frequency shift correlates with the charge on the droplets and is a signature of charge transfer between water and oi (Fig. 2E)[35]. We use the gray spectrum here as a reference, to identify whether increasing the pH results in a higher frequency shift, and thus an increase in charge transfer. Comparing the C-H mode spectra recorded at pD 7 and pD 11 in Fig. 2C, no additional frequency shift is observed at higher pH. Therefore, Figs. 2C and 2D show that neither the interfacial structure of the H-bond network of water, nor the amount of charge transfer is pH-dependent. We also note that, had there been adsorption of OH^- or other ions, this would have led to significant changes in the SHS scattering patterns and the SFS spectra[31]. The absence of interfacial OH^- agrees with a recent Raman MCR study that showed OH^- being excluded from the hydration shells of small hydrophobic molecules (with pH > 12)[46]. Thus, we observe that interchanging Cl^- and OH^- does not result in additional surface charge or in a change of interfacial interactions. Furthermore, the oil and water surface structure are identical for both cases. Therefore, an increase in droplet mobility (Fig. 1C) cannot originate from an increase in surface charge density, as suggested by considering only ionic species as charge carriers within the classical theory.

A classical description of charge is insufficient

As noted, there are several reasons why a classical description of the electrostatics is insufficient: The interfacial charge on the oil droplet (~0.015 e^-/nm^2)[37] arises from improper H-bonds between C-H and O-H groups[35], as sketched in Fig. 2E. These H-bonds emerge from a combination of interactions involving charge transfer and Pauli repulsion[47] among others, which are clearly only well described on the quantum level. Their individual strength is weak (< kT) but since there are many, it results in a sizable total charge density. Furthermore, charge transport in basic solutions is fundamentally different from that in chloride solutions. Cl^- ions are symmetrically hydrated, while OH^- are solvated asymmetrically maximizing the number of H-bonds in which they are involved. The OH^- ion is a topological H-bond network defect that has a hydrophilic side that accepts up to 4 H-bonds and a hydrophobic side that donates a weak H-bond[48]. Thanks to these defect structures, the H-bond network itself becomes a more

efficient conduit for charge transport, with charge transferring via the Grotthuss mechanism by means of H-bond network correlations[29]. This difference is illustrated in Fig. 3A. As a consequence, dilute OH⁻ solutions conduct charge x ~2 faster than dilute Cl⁻ solutions: The charge conductivity, σ, is 244.60 S cm^2/mol for 1 mM NaOH in water and 123.68 S cm^2/mol for 1 mM NaCl[49], even though their dielectric constant and viscosity are identical. Given a certain applied electrostatic field (E), the current density $j = \sigma \cdot E$ is x ~2 bigger, which means that the solutions' polarization P must also be bigger (since $j = \frac{dP}{dt}$). Therefore, we next investigate the charge distribution in hydroxide and chloride solutions under the influence of an electrostatic field using quantum level ab-initio molecular dynamics simulations (AIMD).

Quantum level insights into the charge distributions in bulk solutions

To visualize the electron density, we computed the Wannier centers of the Cl⁻ and OH⁻ ions in bulk liquid water, with and without the application of an external field of 10^8 V/m (more details in the SI).
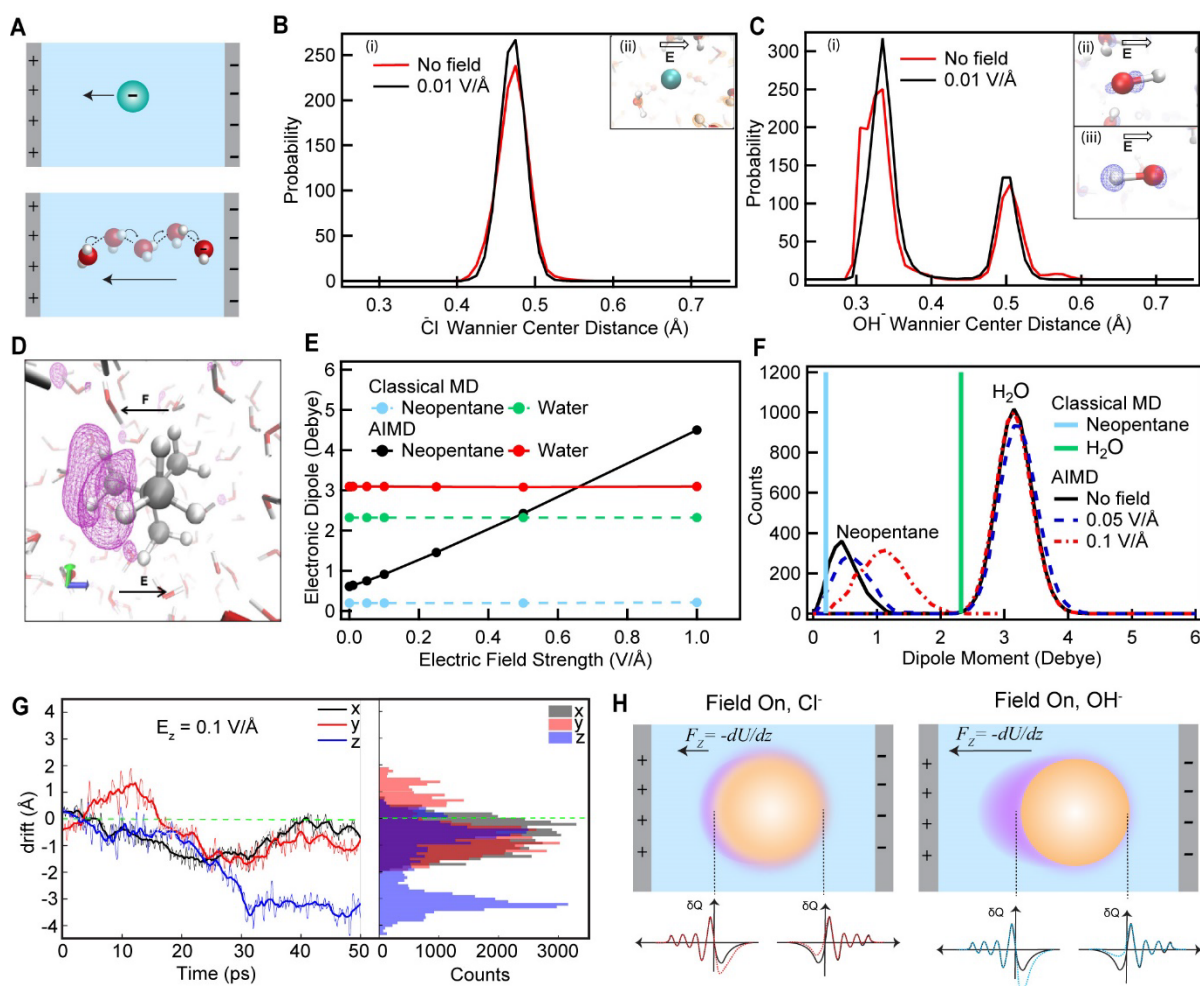
Figure 3. Droplet mobility arises from electron density fluctuations. (A) Illustration of the difference between charge transport in a bulk solution containing chloride (top, hydrodynamic flow), or hydroxide ions (bottom, Grotthuss mechanism, correlated H-bonds). (B) Wannier Center-Cl^- distance distribution shown in black and red with and without field, respectively (i), and snapshot of the response of the electron density around Cl^- upon application of an external electric field (ii). (C) Wannier Center-OH^- distance distribution shown in black and red with and without electric field, respectively (i), and snapshot of the response of the electron density around OH^- upon application of an external electric field (ii). The arrows represent the direction of the electrostatic field. (D) Change of the Hartree potential (iso-value equal to 0.002 e-*Ha/Å) of neopentane when an electrostatic field of magnitude 0.1 V/Å is turned on in the z-direction. The resulting force is indicated with an arrow. (E) Dipole moment of neopentane and water as a function of the external electric field strength, using a classical or quantum mechanical representation of the molecules. (F) Distribution of dipole moments in the solution for both the classical and quantum mechanical representations. Note that due to the high-level requirements on the computations in panels B-G, we employ a field strength that is significantly higher than in the experiment, but well below any threshold for chemical modification[50] (G) Cartesian components of the drift of the C atoms of the neopentane molecule under the action of a 0.1 V/Å field oriented along the z-axis. Negative values of the z-component of the drift (magnified in the blue histogram on the right) give further evidence of the importance of mobile electron density fluctuations on neopentane in the presence of an external field and are the consequence of the force shown in panel D. (H) (left): Schematic illustration of change in charge distribution on an oil nanodroplet in water when an external electrostatic field is applied (dashed lines, bottom). (right): Additional asymmetry is induced due to the difference in polarizability of the bulk basic solution in the presence of an external electrostatic field.

Figures 3B and 3C compare the distributions of the Wannier centers with respect to the O atom in the case of the Cl^- or OH^- ion shown with and without the field in black and red, respectively. In the case of the Cl^- ion, the presence of a single peak witnesses the spherical symmetry of the local electron density, while the OH^- ion is characterized by two different sets of Wannier orbitals. For the OH^- ion, these two Wannier orbitals correspond to the lone pair electrons and those residing along the covalent bond shared between the oxygen and the proton. Comparing hydrated Cl^- and OH^-, we find that an external electrostatic field increases the amount of locally displaced charge density in OH^- solutions more than when compared to Cl^- solutions. Furthermore, OH^- solutions display a large amount of charge density asymmetry in the direction of the field, while for Cl^- solutions there is no field-induced directionality, consistent with the asymmetric response of the local H-bonds observed for OH^- solutions. Thus, at identical ionic strengths, external fields induce a different response in the electronic polarization for pH neutral and basic solutions.

Mobile surface and bulk electron density fluctuations drive electrophoresis

Next, we investigate on the quantum molecular level, what the effect of an external electrostatic field (E) is on a hydrophobic nano-object in water. To this end, we conducted Density Functional Theory (DFT) simulations of a hydrophobic molecule, neopentane (C_5H_{12}) in liquid water. We begin by showing in Fig. 3D the change of the Hartree potential as obtained from the simulations of a single neopentane molecule in water, in the presence of an applied oriented external field. The electric field induces a sizable asymmetry in the potential across the neopentane molecule and along the field direction, as indicated by the purple isolines in Fig. 3D. This type of electronic polarization is not included in any classical description used to rationalize hydrodynamic flow. To illustrate this point, we compared the evolution of the dipole moment of hydrated neopentane obtained from a classical point charge, but flexible model, to

11

our AIMD simulations. Fig. 3E shows that upon introducing an electric field on the optimized structure at 0 K, the electronic dipole moment of the neopentane molecule grows from 0.5 D at zero field to 1.5 D at a field strength of 0.5 V/Å whereas, in the classical model, the dipole is close to zero and fully independent from the applied field strength. This evidence shows that there are important electronic polarization effects involving the neopentane molecule in the presence of the field. In addition to the bare electronic response at 0 K, Fig. 3F shows the results of AIMD simulations at finite temperature. It can be seen that the electric field significantly enhances the polarizability of the neopentane molecule in water. This is consistent with recent work using both DFT and many-body polarizable potentials showing that the dipole moment of methane increases under pressure[51,52], and to a lesser extent, under strong electric fields[53].

Thus, external electric fields induce electronic charge separations in hydrophobic molecules (Fig. 3D-F), and in hydroxide solution (Fig. 3C) when they are considered on the quantum mechanical level. Having induced a mobile charge separation ($\frac{dP}{dt}$), an electric field induced energy gradient and thus force ($F_z = -\frac{dU}{dz}$) emerges naturally. Namely, when an external electrostatic field ($\boldsymbol{E} = E_z$, Fig. 3D) interacts with charge density fluctuations ($\frac{dP}{dt}$), electrodynamic work ($\int (J.E)dr^3 = \int (\frac{dP}{dt} \cdot E)dr^3$) is done[54]. This force can be verified by mapping the speed of the neopentane with the external field on (Fig. 3G) and field off (Fig. S3). Indeed, the neopentane drifts in the opposite direction of the field (while it does not do so when the field is off), leading to a mobility of $\mu \sim$ -1· 10^{-8} m^2/Vs, which is in very good agreement with the experiment (Fig. 1C) given that the size of the system, the field strength and time lapse of the simulation are all scaled to the molecular dimension in the simulations. Although it is well known that charge gradients in external fields (or field gradients with fixed charge distributions) give rise to forces, as e.g. manifested in dielectrophoresis[55] or electrorotation[56], the force discussed here cannot result in any way from a purely classical continuum treatment.

Turning now to the oil droplet motion, we can explain both its stability, its mobility and why the pH change leads to more than a duplication of the mobility (Fig. 1D), while at the same time surface charge and charge transfer of a whole droplet are not impacted (Fig. 1F, Fig. 2C, D). In absence of an electrostatic field, the droplet interface experiences electron charge density fluctuations that originate from H-bond dynamics at the interface (both from improper C-H…O bonds, and O-H…O bonds, Fig. 2E). This results in a net negative charge, which ensures that the droplets are stable against coalescence. Based on the results of Fig. 3B-G, we propose that an external electrostatic field changes the charge distribution on either side of the droplet interface, somewhat depleting the negative charge on the side of the negative electrode, and enhancing it on the side of the positive electrode (Fig. 3H, left). In analogy to

the neopentane case, there is an electrodynamic polarization and an energy gradient, which constitutes a net force. In basic solutions, this charge asymmetry / polarization gradient is enhanced (Fig. 3H, right) by ~x 2 since the charge conductivity (and current density / change in polarizability) is larger by that amount, and it couples directly to the electromagnetic energy. This results in a larger amount of work / force, and a larger droplet mobility, which increases in the same way as the increase in bulk conductivity.

Summary

Remarkably, numerous different experiments on varying surface chemistries display very similar pH dependent effects. Here, we provided a general framework for rationalizing the origins of these phenomena. A classical continuum model description of electrophoretic phenomena breaks down under the very general case when the pH of the solution is varied. We measured electrophoretic mobility of hydrophobic nanoscale oil droplets in water and combined it with nonlinear optical spectroscopic measurements as a function of pH. Surface potential and charge was measured as a function of pH under conditions of constant ionic strength whereby Cl^- and OH^- were interchanged. We also used vibrational sum frequency scattering to determine the pH-dependent molecular interfacial structure and interactions. While the mobility increased drastically upon increasing the pH, neither did the surface potential, nor the interfacial interactions. In other words, the surface charge turned out to be pH-independent. AIMD simulations of chloride and hydroxide ions in water showed that applying an electrostatic field across solutions of OH^- and Cl^- ions leads to a different polarization, with an electron density distribution that is both enhanced and anisotropic for OH^-, but not for Cl^-. DFT simulations of neopentane in water with an external electric field show an electronic charge polarization within the molecule, which is proportional to the external field strength. Combining experimental findings and quantum level considerations, we arrive at a description of an electric field-induced force that originates from gradients in the fluctuating electric polarizability of the droplet surface, which ultimately arises from charge transfer-induced electron density fluctuations. The induced charge density gradient interacts with an external electric field, which results in a force as it represents a gradient in the electrodynamic energy distribution. This force was manifest on the neopentane, as it induced a mobility of the same order of magnitude as measured in the nanodroplets. In basic solutions, this charge asymmetry / polarization gradient is enhanced by ~x 2 because the charge conductivity (and thus current density / change in polarizability) is larger by exactly that amount, and it couples to the electromagnetic energy. This mechanism is very general and impacts many processes in biology, chemistry, and nanotechnology and provides an explanation of why bulk acidity or basicity can have important implications in transport phenomena.

13

Author contributions:

Experiments: SP, SK, TS

Data interpretation: SP, SR

MD Simulations: GC

Analysis of MD simulations: GC, SR, AH

Conception and Supervision: SR

Writing: SR, SP, GC, AH

Competing interests:

Authors declare that they have no competing interests.

Data and materials availability:

All data in the manuscript and SI are available through Zenodo

References

1   Ohshima, H. *Theory of Colloid and Interfacial Electric Phenomena*. (Elsevier Academic Press, 2006).

2   Bocquet, L. & Charlaix, E. Nanofluidics, from bulk to interfaces. *Chem. Soc. Rev.* **39**, 1073-1095 (2010).

3   Eijkel, J. C. T. & Berg, A. v. d. Nanofluidics: what is it and what can we expect from it? *Microfluid Nanofluid* **1**, 249-267 (2005).

4   Haywood, D. G., Saha-Shah, A., Baker, L. A. & Jacobson, S. C. Fundamental Studies of Nanofluidics: Nanopores, Nanochannels, and Nanopipets. *Anal. Chem.* **87**, 172-187 (2015).

5   Karniadakis, G., Beskok, A. & Aluru, N. *Microflows and Nanoflows Fundamentals and Simulation*. 1 edn, (Springer, 2005).

6   Bonthuis, D. J. & Netz, R. R. Beyond the Continuum: How Molecular Solvent Structure Affects Electrostatics and Hydrodynamics at Solid–Electrolyte Interfaces. *J. Phys. Chem. B.* **117**, 11397-11413 (2013).

7   Rezaei, M. *et al.* Interfacial, Electroviscous, and Nonlinear Dielectric Effects on Electrokinetics at Highly Charged Surfaces. *J. Phys. Chem. B.* **125**, 4767-4778 (2021).

8   Matyushov, D. V. Electrophoretic mobility without charge driven by polarisation of the nanoparticle–water interface. *Mol. Phys.* **112**, 2029-2039 (2014).

9   Bouzigues, C. I., Tabeling, P. & Bocquet, L. Nanofluidics in the Debye Layer at Hydrophilic and Hydrophobic Surfaces. *Phys. Rev. Lett.* **101**, 114503 (2008).

10   Huang, D. M., Sendner, C., Horinek, D., Netz, R. R. & Bocquet, L. Water Slippage versus Contact Angle: A Quasiuniversal Relationship. *Phys. Rev. Lett.* **101**, 226101 (2008).

11   Geng, X. *et al.* Slip length and structure of liquid water flowing past atomistic smooth charged walls. *Sci Rep* **9**, 18957 (2019).

12   Ohshima, H. Electrophoretic mobility of a liquid drop with a slip surface. *Colloid Polym. Sci* **299**, 1353-1356 (2021).

13   Kavokine, N., Bocquet, M.-L. & Bocquet, L. Fluctuation-induced quantum friction in nanoscale water flows. *Nature* **602**, 84-90 (2022).

14   Mahapatra, P., Ohshima, H. & Gopmandal, P. P. Electrophoresis of Dielectric and Hydrophobic Spherical Fluid Droplets Possessing Uniform Surface Charge Density. *Langmuir* **38**, 11421-11431 (2022).

15   Mahapatra, P., Ohshima, H. & Gopmandal, P. P. Effect of hydrodynamic slip on the electrophoresis of hydrophobic spherical particles in a solution of general electrolytes. *Colloid Polym Sci* **300**, 1311-1325 (2022).

16   Siria, A. *et al.* Giant osmotic energy conversion measured in a single transmembrane boron nitride nanotube. *Nature* **494**, 455-458 (2013).

17   Secchi, E., Niguès, A., Jubin, L., Siria, A. & Bocquet, L. Scaling Behavior for Ionic Transport and its Fluctuations in Individual Carbon Nanotubes. *Phys. Rev. Lett.* **116**, 154501 (2016).

18   Hong, S. *et al.* Scalable Graphene-Based Membranes for Ionic Sieving with Ultrahigh Charge Selectivity. *Nano Lett.* **17**, 728-732 (2017).

19   Feng, J. *et al.* Single-layer MoS2 nanopores as nanopower generators. *Nature* **536**, 197-200 (2016).

20   Agmon, N. *et al.* Protons and Hydroxide Ions in Aqueous Systems. *Chem. Rev.* **116**, 7642-7672 (2016).

21   Beattie, J. K. & Djerdjev, A. M. The Pristine Oil/Water Interface: Surfactant-Free Hydroxide-Charged Emulsions. *Angew. Chem. Int. Ed.* **43**, 3568-3571 (2004).

22   Jabłoński, J., Janusz, W. & Szczypa, J. Adsorption properties of the stearic acid-octadecane particles in aqueous solutions. *J. Dispersion Sci. Technol.* **20**, 165-175 (1999).

23   Li, C. & Somasundaran, P. Reversal of bubble charge in multivalent inorganic salt solutions—Effect of magnesium. *J. Colloid Interface Sci.* **146**, 215-218 (1991).

24   Lützenkirchen, J., Preočanin, T. & Kallay, N. A macroscopic water structure based model for describing charging phenomena at inert hydrophobic surfaces in aqueous electrolyte solutions. *Phys. Chem. Chem. Phys.* **10**, 4946-4955 (2008).

25   Marinova, K. G. *et al.* Charging of Oil−Water Interfaces Due to Spontaneous Adsorption of Hydroxyl Ions. *Langmuir* **12**, 2045-2051 (1996).

26   Yang, C., Dabros, T., Li, D., Czarnecki, J. & Masliyah, J. H. Measurement of the Zeta Potential of Gas Bubbles in Aqueous Solutions by Microelectrophoresis Method. *J. Colloid Interface Sci.* **243**, 128-135 (2001).

27   Snapp, P. *et al.* Interaction of 2D materials with liquids: wettability, electrochemical properties, friction, and emerging directions. *NPG Asia Mater* **12**, 22 (2020).

28   Kunz, W. *Specific Ion Effects*. (WORLD SCIENTIFIC, 2009).

29   Tuckerman, M. E., Chandra, A. & Marx, D. Structure and Dynamics of OH-(aq). *Acc. Chem. Res.* **39**, 151-158 (2006).

30   Agmon, N. The Grotthuss mechanism. *Chem. Phys. Lett.* **244**, 456-462 (1995).

31   Jena, K. C., Scheu, R. & Roke, S. Surface Impurities Are Not Responsible For the Charge on the Oil/Water Interface: A Comment. *Angew. Chem. Int. Ed.* **51**, 12938-12940 (2012).

32   Yan, X. *et al.* Central Role of Bicarbonate Anions in Charging Water/Hydrophobic Interfaces. *J. Phys. Chem. Lett.* **9**, 96-103 (2018).

33   Roger, K. & Cabane, B. Why Are Hydrophobic/Water Interfaces Negatively Charged? *Angew. Chem. Int. Ed.* **51**, 5625-5628 (2012).

34   Uematsu, Y., Bonthuis, D. J. & Netz, R. R. Nanomolar Surface-Active Charged Impurities Account for the Zeta Potential of Hydrophobic Surfaces. *Langmuir* **36**, 3645-3658 (2020).

35   Pullanchery, S., Kulik, S., Rehl, B., Hassanali, A. & Roke, S. Charge transfer across C–H⋯O hydrogen bonds stabilizes oil droplets in water. *Science* **374**, 1366-1370 (2021).

36   Samson, J.-S., Scheu, R., Smolentsev, N., Rick, S. W. & Roke, S. Sum frequency spectroscopy of the hydrophobic nanodroplet/water interface: Absence of hydroxyl ion and dangling OH bond signatures. *Chem. Phys. Lett.* **615**, 124-131 (2014).

37   Poli, E., Jong, K. H. & Hassanali, A. Charge transfer as a ubiquitous mechanism in determining the negative charge at hydrophobic interfaces. *Nat. Commun.* **11**, 901 (2020).

38   Lütgebaucks, C., Gonella, G. & Roke, S. Optical label-free and model-free probe of the surface potential of nanoscale and microscopic objects in aqueous solution. *Phys. Rev. B* **94**, 195410 (2016).

39   de Beer, A. G. F., Campen, R. K. & Roke, S. Separating surface structure and surface charge with second-harmonic and sum-frequency scattering. *Phys. Rev. B* **82**, 235431 (2010).

40   Bischoff, M., Biriukov, D., Předota, M., Roke, S. & Marchioro, A. Surface Potential and Interfacial Water Order at the Amorphous TiO2 Nanoparticle/Aqueous Interface. *J. Phys. Chem. C.* **124**, 10961-10974 (2020).

41   Marchioro, A. *et al.* Surface Characterization of Colloidal Silica Nanoparticles by Second Harmonic Scattering: Quantifying the Surface Potential and Interfacial Water Order. *J. Phys. Chem. C.* **123**, 20393-20404 (2019).

42   Pullanchery, S., Kulik, S., Okur, H. I., de Aguiar, H. B. & Roke, S. On the stability and necessary electrophoretic mobility of bare oil nanodroplets in water. *J. Chem. Phys.* **152**, 241104 (2020).

43   de Aguiar, H. B., Samson, J.-S. & Roke, S. Probing nanoscopic droplet interfaces in aqueous solution with vibrational sum-frequency scattering: A study of the effects of path length, droplet density and pulse energy. *Chem. Phys. Lett.* **512**, 76-80 (2011).

44   Pullanchery, S., Kulik, S. & Roke, S. Water Structure at the Hydrophobic Nanodroplet Surface Revealed by Vibrational Sum Frequency Scattering Using Isotopic Dilution. *J. Phys. Chem. B.* **126**, 3186-3192 (2022).

45   Chen, Y., Jena, K. C., Lütgebaucks, C., Okur, H. I. & Roke, S. Three Dimensional Nano "Langmuir Trough" for Lipid Studies. *Nano Lett.* **15**, 5558-5563 (2015).

46   Bredt, A. J. *et al.* Expulsion of Hydroxide Ions from Methyl Hydration Shells. *J. Phys. Chem. B.* **126**, 869-877 (2022).

47   Mao, Y. *et al.* From Intermolecular Interaction Energies and Observable Shifts to Component Contributions and Back Again: A Tale of Variational Energy Decomposition Analysis. *Annu. Rev. Phys. Chem.* **72**, 641-666 (2021).

48   Crespo, Y. & Hassanali, A. Unveiling the Janus-Like Properties of OH–. *J. Phys. Chem. Lett.* **6**, 272-278 (2015).

49   CRC handbook of chemistry and physics.   (1977).

50   Cassone, G. Nuclear Quantum Effects Largely Influence Molecular Dissociation and Proton Transfer in Liquid Water under an Electric Field. *J. Phys. Chem. Lett.* **11**, 8983-8988 (2020).

51   Pruteanu, C. G. *et al.* Squeezing Oil into Water under Pressure: Inverting the Hydrophobic Effect. *J. Phys. Chem. Lett.* **11**, 4826-4833 (2020).

52   Robinson, V. N. *et al.* The behavior of methane–water mixtures under elevated pressures from simulations using many-body potentials. *J. Chem. Phys.* **156**, 194504 (2022).

53   Cassone, G., Sponer, J. & Saija, F. Molecular dissociation and proton transfer in aqueous methane solution under an electric field. *Phys. Chem. Chem. Phys.* **23**, 25649-25657 (2021).

54   Jackson, J. D. *Classical electrodynamics*. (Third edition. New York : Wiley, [1999] ©1999, 1999).

55   Sarno, B., Heineck, D., Heller, M. J. & Ibsen, S. D. Dielectrophoresis: Developments and applications from 2010 to 2020. *ELECTROPHORESIS* **42**, 539-564 (2021).

56   Huang, L., Zhao, P., Liang, F. & Wang, W. in *Methods Cell Biol.* Vol. 148 (eds Daniel A. Fletcher, Junsang Doh, & Matthieu Piel) 97-116 (Academic Press, 2018).

Supplementary Information for

pH drives electron density fluctuations that enhance electric field-induced liquid flow

S. Pullanchery, S. Kulik, T. Schönfeldová, G. Cassone, A. Hassanali, S. Roke

This PDF file includes:

Materials and Methods (S1)

Supplementary Text

Figs. S1 – S3

Table S1-S4

S1. Materials and Methods

Chemicals

Hexadecane (highest available analytical standard, Sigma Aldrich, < 5 mL vials), D_2O (99.8% atom % D, Acros Organics), sulfuric acid (95-97%, Merck), H_2O_2 (30%, Reactolab SA), d_{75}-DPPC (Avanti Polar Lipids), NaCl (99.999%, Acros), NaOH (99.99%, Sigma-Aldrich), and NaOD solution (40 wt.% in D_2O, 99.5 at.% D, Sigma-Aldrich), were used as received. The purity of hexadecane was verified with a Zisman test[1]. The glassware used to prepare and store the nanodroplets was freshly taken out of the manufacturer's packaging and never reused after the preparation. As a first step, the glassware was cleaned with a freshly prepared piranha (3:1 H_2SO_4:H_2O_2) solution. After being immersed in the piranha solution for ~45 minutes, the glassware was rinsed copiously with ultrapure water (18.2 MΩ ·cm), obtained from a Milli-Q UF-Plus instrument (Millipore Inc.)

Oil Nanodroplets in Water

As described previously[2], mixtures of 2 vol% hexadecane in pure H_2O or D_2O were first mixed for ~3 minutes using a vortexer (IKA® Vortex 2). These mixtures were then ultrasonicated (35 kHz, 400 W, Bandelin) until monodisperse droplets with diameters in the appropriate size range were formed, and diluted as required by the different experiments. The size distributions of the nanodroplets were characterized by dynamic light scattering (DLS) using a Malvern Zetasizer Ultra instrument. The size distribution of hexadecane droplets in water with 1 mM NaCl and 1 mM NaOH is shown in Fig. S1.
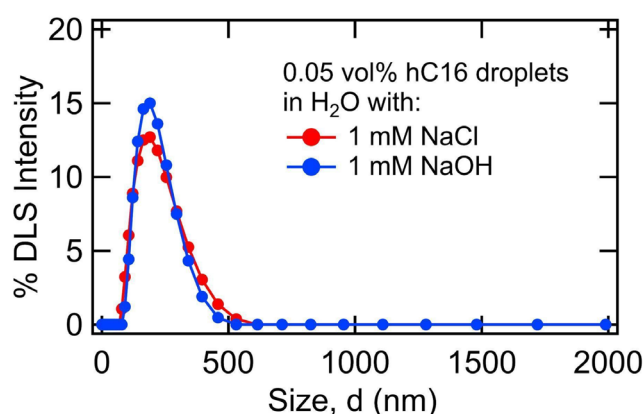

Fig. S1. Oil droplet size distribution. DLS intensity distribution as a function of diameter of 0.05 vol % hexadecane droplets prepared in water with 1 mM NaCl (red curve) and 1 mM NaOH (blue curve). The PDI of the curves correspond to 0.2 (NaCl) and 0.2 (NaOH), respectively.

Oil droplets covered with d-DPPC (Fig. 1F) were prepared by mixing 2 vol% hexadecane with D_2O containing 1 mM lipid. The mixture was then homogenized for 2 minutes with a hand-held homogenizer (TH, OMNI International) using an angular velocity of 15 rpm and subsequently

placed in an ultrasonic bath (35 kHz, 400 W, Bandelin) until monodisperse droplets were formed.

Electrokinetic mobility measurements

The electrophoretic mobility measurements were performed using laser Doppler velocimetry and phase analysis light scattering, employing a dynamic light scattering instrument (Malvern Zetasizer Ultra). To perform the electrophoretic mobility the nanoemulsions were diluted to 0.05 vol% by adding ultrapure water. The electrophoretic mobility (μ) values were converted into ζ-potential (ζ) values using the following expression: $\mu = \frac{\epsilon_0 \epsilon \zeta f(\kappa R)}{\eta}$ where ϵ_0 is the vacuum permittivity, ϵ is the relative permittivity of water (78.17), η the viscosity of water (0.89 cP), $f(\kappa R)$ is Henry's function, κ is the inverse Debye length ($\sqrt{\epsilon_0 \epsilon k_B T / 2.10^3 N_A e^2 I}$, where k_B is the Boltzmann constant, T is the temperature, N_A is the Avogadro's number, e is the elementary charge and I is ionic strength), and R is the radius of the droplet. The typical approximations used for Henry's function are the Smoluchowski formula in which $f(\kappa R) \rightarrow 1$, and the Hückel formula in which $f(\kappa R) \rightarrow 2/3$. In the case of oil droplets in water, we use a more generalized form proposed by Oshima[3] for Henry's function:

$$f(\kappa R) \;=\; \frac{2}{3}\left[1 + \frac{1}{2\left\{1 + \frac{2.5}{\kappa R(1 + 2e^{-\kappa R})}\right\}^3}\right] \tag{S1}$$

Note that this assumes no slip as a boundary condition.

Angle-resolved second harmonic scattering

SHS measurements were performed using 190-fs laser pulses centered at 1028 nm with a 200kHz repetition rate. The polarization of input pulses was controlled by a Glan-Taylor polarizer (GT10-B, Thorlabs) in combination with a zero-order half-wave plate (WPH05M-1030). The filtered (FEL0750, Thorlabs) input pulses with a pulse energy of 0.3 μJ (incident laser power P = 60 mW) were focused into a cylindrical glass sample cell (inner diameter 4.2 mm) with a waist diameter of ~35 μm and a Rayleigh length of 0.94 mm. The scattered second harmonic light was collected with a plano-convex lens (f = 5 cm), and then filtered (ZET514/10x, Chroma), polarized (GT10-A, Thorlabs), and finally focused into a gated photomultiplier tube (H7421-40, Hamamatsu). The angle of acceptance for the signal collection was 3.4°. The scattering pattern was measured at a scanning step of 5°, between -90° < θ < 90°. Each data point was acquired with an acquisition time of 20 × 1 s and a gate width of 10 ns. All measurements were performed in a temperature- and humidity-controlled

room (T = 297 K; relative humidity, 26.0 %). The normalized SHS intensity $S(\theta)$ at the angle θ was calculated as:

$$S(\theta) = \frac{I(\theta)_{sample}^{PXX} - I(\theta)_{solvent}^{PXX}}{I(\theta)_{H2O}^{SSS}} \tag{S2}$$

where $I(\theta)_{sample}^{PXX}$ and $I(\theta)_{solvent}^{PXX}$ are the average SHS intensities of the sample and solvent at the same given temperature, respectively. $I(\theta)_{H2O}^{SSS}$ is the average SHS intensity of water at room temperature. The XX stands for the polarization state of the incident beam relative to the scattering plane (P - parallel or S - perpendicular). Because bulk water is used as normalizing substance all the measured patterns can be compared in their intensity, with an error in the intensity of 1-2 %[4].

The computed $S(\theta)$ curves (black lines) in Fig.1F were obtained using nonlinear light scattering theory, described in detail in Refs[5,6]. The equations used to relate $S(\theta)$ to the surface potential are derived using the Rayleigh-Gans-Debye (RGD) approximation, in the absence of multiple scattering, with a first-order correction for the jump in the electromagnetic field amplitude across the interface[7]. Equations S3 and S4 are derived by considering the following assumptions[5,6,8]:

- The liquid can be considered spatially isotropic in the azimuthal direction. This ensures that only 4 of the possible 81 elements of the $\chi^{(3)\prime}$ and $\Gamma^{(3)\prime}$ tensors are non-zero.
- The particle interface can be considered isotropic in the interfacial plane. This reduces the complexity such that only 4 elements of the $\chi_s^{(2)}$ and $\Gamma^{(2)}$ are non-zero.
- The sample consists of a lossless nonlinear medium, which means that no energy is transferred from the optical pulses to the material. This leads to the degeneracy of three of the four tensor elements of $\chi_s^{(2)}$ ($\Gamma^{(2)}$), and $\chi^{(3)\prime}$($\Gamma^{(3)\prime}$), so that only the pair $(\chi_1^{(2)}, \chi_2^{(2)})$, and $\chi_2^{(3)\prime}$ are left as non-zero.
- The orientation distribution of water molecules at the interface is broad. Under these conditions, the tensor element $\chi_{s,1}^{(2)}$ becomes negligible.

The equations that relate $S(\theta)$ to R, Φ_0 and $\chi_{s,2}^{(2)}$ are given in Ref.[6] (Equations 2 and 3, and Tables 2 and 3). This formalism was later modified for water-in-oil droplets, where contributions from both the inside aqueous and outside oil interfaces were considered[9]. Here, we adapt a similar approach to calculate scattering patterns that take into account both the oil and water contributions from the oil/water interface. In this formalism, the scattered intensity for the two independent polarization combinations PPP and PSS can be expressed as:

$$S_{PPP}(\theta) = \frac{I_{PPP}(\theta)}{I_{SSS}(\theta)} = \frac{\varepsilon_0^2 \left(E_P(\omega)^2 \left[\cos\left(\frac{\theta}{2}\right)^3 \left(\Gamma_{1,oil}^{(2)} - \Gamma_{1,H_2O}^{(2)} \right) + \cos\left(\frac{\theta}{2}\right) \left(\left(\Gamma_{2,oil}^{(2)} - \Gamma_{2,H_2O}^{(2)} \right) + \left(\Gamma_{2,H_2O}^{(3)\prime} + \Gamma_{2,oil}^{(3)\prime} \right) \right) (2\cos(\theta)+1) \right] \right)^2}{\bar{\mu}^2 N_b / N_p}$$

(S3)

$$S_{PSS}(\theta) = \frac{I_{PSS}(\theta)}{I_{SSS}(\theta)} = \frac{\varepsilon_0^2 \left(E_S(\omega)^2 \left[\cos\left(\frac{\theta}{2}\right) \left(\left(\Gamma_{2,oil}^{(2)} - \Gamma_{2,H_2O}^{(2)} \right) + \left(\Gamma_{2,H_2O}^{(3)\prime} + \Gamma_{2,oil}^{(3)\prime} \right) \right) \right] \right)^2}{\bar{\mu}^2 N_b / N_p}$$

(S4)

where $\Gamma_{1,H_2O}^{(2)}$, $\Gamma_{2,H_2O}^{(2)}$, and $\Gamma_{2,H_2O}^{(3)\prime}$ are the effective particle susceptibilities of water, and $\Gamma_{1,oil}^{(2)}$, $\Gamma_{2,oil}^{(2)}$, and $\Gamma_{2,oil}^{(3)\prime}$ are the effective particle susceptibilities of the oil inside the droplet. $\bar{\mu} = \bar{\beta}_{H_2O}^{(2)} E(\omega)^2$ is the average induced second-order dipole moment with $\bar{\beta}_{H_2O}^{(2)}$ the averaged hyperpolarizability of water. N_p is the number of droplets and N_b is the density of bulk water (3.34×10^{28} molecules/m³). The elements of the nonlinear effective particle susceptibility are related to the surface susceptibility according to the expressions in table S1.

Table S1: Analytical expressions used for computing equations S3 and S4 comprised of the surface and particle susceptibility elements of the interface, the form factor functions and the scattering vector.

Susceptibility elements outside the droplet	Susceptibility elements inside the droplet
$\chi_{s,1}^{(2)\prime\prime} = 27\eta \dfrac{\left(\chi_{s,1}^{(2)} \eta^2 + 3\chi_{s,2}^{(2)}(\eta^2 - 1) \right)}{(2+\eta)^3}, \eta = \left(\dfrac{n_p}{n_{H_2O}} \right)^2$	$\Gamma_1^{(2)} = 0$
$\chi_{s,2}^{(2)\prime\prime} = 27\eta \dfrac{\chi_{s,2}^{(2)}}{(2+\eta)^3}$	$\Gamma_2^{(2)} = 0$
$\chi_2^{(3)\prime\prime} = 27\eta \dfrac{\chi_2^{(3)\prime}}{(2+\eta)^3}, \chi_2^{(3)\prime} = \dfrac{N_b}{\varepsilon_0}\left(\bar{\beta}^{(3)} + \dfrac{\bar{\beta}^{(2)}\mu_{dc}}{3k_B T} \right)$	$\Gamma_2^{(3)\prime} = 2\chi_2^{(3)\prime\prime} \Phi_0(F_1(qR))$
$\Gamma_1^{(2)} = (2F_1(qR) - 5F_2(qR))\chi_{s,1}^{(2)\prime\prime}$	$\chi_2^{(3)\prime\prime} = 27\eta \dfrac{\chi_2^{(3)\prime}}{(2+\eta)^3}, \chi_2^{(3)\prime} = \dfrac{N_b}{\varepsilon_0}\left(\bar{\beta}^{(3)} \right)$
$\Gamma_2^{(2)} = F_2(qR)\chi_{s,1}^{(2)\prime\prime} + 2F_1(qR)\chi_{s,2}^{(2)\prime\prime}$	
$\Gamma_2^{(3)\prime} = 2\chi_2^{(3)\prime\prime} \Phi_0(F_1(qR) + F_3(qR, \kappa R))$	

Table S2: Analytical expressions of the form factor functions and the scattering vector used for computing equations S3 and S4.

Form factor functions and scattering vector
$$F_1(qR) = 2\pi R^2 i \left(\frac{sin(qR)}{(qR)^2} - \frac{cos(qR)}{qR} \right)$$
$$F_2(qR) = 4\pi R^2 i \left(3\frac{sin(qR)}{(qR)^4} - 3\frac{cos(qR)}{(qR)^3} - \frac{sin(qR)}{(qR)^2} \right)$$
$$F_3(qR, \kappa R) = 2\pi R^2 i \frac{qRcos(qR) + \kappa Rsin(qR)}{(qR)^2 + (\kappa R)^2}$$
$$q = k_0 - 2k_1, \quad q = \left| \frac{4\pi\eta_{H_2O}}{\lambda_{SH}} sin\frac{\theta}{2} \right|$$

The parameters used to compute the SHS scattering patterns of oil droplets in water (Fig. 1F) are given in table S4.

Table S3: Constants and equalities used in equations S3 and S4 (*16*)

Constants and equalities
$$\mu_{dc} = 8.97 \times 10^{-30} \; Cm$$
$\bar{\beta}^{(2)} = 3.09 \times 10^{-52} \; C^3m^3J^{-2}$ for H_2O
$\bar{\beta}^{(3)} = 4.86 \times 10^{-62} \; C^4m^4J^{-3}$ for H_2O
$\bar{\beta}^{(3)} = 7.09 \times 10^{-61} \; C^4m^4J^{-3}$ for n-$C_{16}H_{34}$ [10]
$$\chi_{s,1}^{(2)} = \chi_{s,\perp\perp\perp}^{(2)} - \chi_{s,\|\|\perp}^{(2)} - \chi_{s,\|\perp\|}^{(2)} - \chi_{s,\perp\|\|}^{(2)}$$
$$\chi_{s,2}^{(2)} = \chi_{s,\|\|\perp}^{(2)}$$
$$\chi_{s,1}^{(2)} = 0$$
$$\chi_{s,4}^{(2)} = \chi_{s,3}^{(2)} = \chi_{s,2}^{(2)}, \; \chi_4^{(3)'} = \chi_3^{(3)'} = \chi_2^{(3)'}$$

Table S4: Parameters used to compute the SHS curves of oil droplets in water

Parameter	Value
SH wavelength, λ_{SH}, nm	514
Refractive index of water, n_{H_2O}	1.333
Refractive index of oil, n_{oil}	1.435
Radius of droplets, R, nm	DLS distribution
Number density of droplets, N_p, mL^{-1}	$1.7 \cdot 10^{10}$
Ionic strength of water, mM	1
Ionic strength of oil, mM	0
Surface susceptibility of water, $\chi^{(2)}_{s,2,H_2O}$, m²/V	$-0.24 \cdot 10^{-22}$
Surface susceptibility of oil, $\chi^{(2)}_{s,2,oil}$, m²/V	0

Vibrational sum frequency scattering

The experimental set-up for the vibrational SFS spectroscopy has been described in detail previously[11,12]. Briefly, an 800 nm regeneratively amplified Ti:sapphire system (Spitfire Pro, Spectra physics) seeded with an 80 MHz 800 nm oscillator (Mai Tai SP) was operated at a 1 kHz repetition rate to pump a commercial OPG/OPA/DFG system (HE-TOPAS-C, Light Conversion), used to generate broadband infrared pulses. The visible beam was split off directly from the amplifier, and spectrally shaped with a home-built pulse shaper. The visible (800 nm, 10 mJ, FWHM 15 cm^{-1}) and the IR (3-4.5 mm, 10 mJ, FWHM 170 cm^{-1}) beams were spatially and temporally overlapped with an IR-VIS opening angle of 15°, in a inside sample cell that had an optical path length of 0.2 mm. At a scattering angle (θ) of 57° as measured in air, the scattered SF light was collimated using a plano-convex lens (f = 15 mm, Thorlabs LA1540-B) and passed through two short-wave pass filters (3rd Millenium, 3RD770SP). The SF light was spectrally dispersed with a monochromator (Acton, SpectraPro 2300i) and detected with an intensified CCD camera (Princeton Instruments, PI-Max3) using a gate width of 10 ns. A Glan-Taylor prism (Thorlabs, GT15-B), a half-wave plate (EKSMA, 460-4215) and a polarizing beam splitter cube (CVI, PBS-800-050) and two BaF$_2$ wire grid polarizers (Thorlabs, WP25H-B) were used to control the polarization of the SF, VIS and infrared beams, respectively. The acquisition time for a single C-H spectrum was 300 s, while the acquisition time for a single D-O spectrum was 600 s. All measurements were performed in a temperature- and humidity-controlled room (T = 297 K; relative humidity, 26.0 %).

The 800 cm^{-1} spectral range of the O-D stretch modes was obtained by recording different SF spectra spaced by 100 cm^{-1} frequency steps. The measured sum frequency spectrum at each frequency range was background subtracted and then normalized with IR and VIS pulse energy and acquisition time. The total SF intensity was computed as a weighted sum of the recorded input spectra (Eq. S1, SI of Ref.[13]), and the resulting intensity was divided

by the IR spectral profile, which was obtained by measuring the SF intensity from a thin film of $BaTiO_3$ nanoparticles. This spectrum is given in Fig. S2, in the SI of Ref.[13].

The effective droplet surface susceptibility ($\Gamma^{(2)}$) spectra, represented by $|\Gamma^{(2)}|^2$ that are shown in Fig. 2B and C and represent the vibrational surface spectrum of the droplets were obtained by performing a computational procedure that takes into account the extinction of the IR light by absorption, and the efficiency of light collection along the optic axis of the collection optics. The theory behind this procedure was described recently in detail in Ref.[14] and its implementation in experiments, together with all the necessary data to do so (frequency-dependent extinction factor, optical response of the focusing geometry) are given in the SM of Ref.[12], section S2 and Figs. S3 and S4.

Examples of the surface chemical sensitivity of SFS

To demonstrate the surface sensitivity of vibrational SFS on the interfacial structure, we show in Fig. S2 SFS spectra of 100 nm d34-hexadecane droplets in aqueous (D_2O) solution. Figs. S2A and S2B show the same droplets, but in contact with 1 mM solutions of zwitterionic phospholipids (1,2-dipalmitoyl-sn-glycero-3-phosphocholine (DPPC) and 1,2-dipalmitoyl-sn-glycero-3-phosphoethanolamine (DPPE), Fig. S2A), as well as charged phospholipids (1,2-dipalmitoyl-sn-glycero-3-phosphate (DPPA), 1,2-dipalmitoyl-sn-glycero-3-phospho-(1'-rac-glycerol) (DPPG), and 1,2-dipalmitoyl-sn-glycero-3-phospho-L-serine (DPPS), Fig. S2B), and a surfactant sodium dodecyl sulfate (SDS). Both panels show very different spectra that report on the different surface structures of the different lipid acyl chains [15].
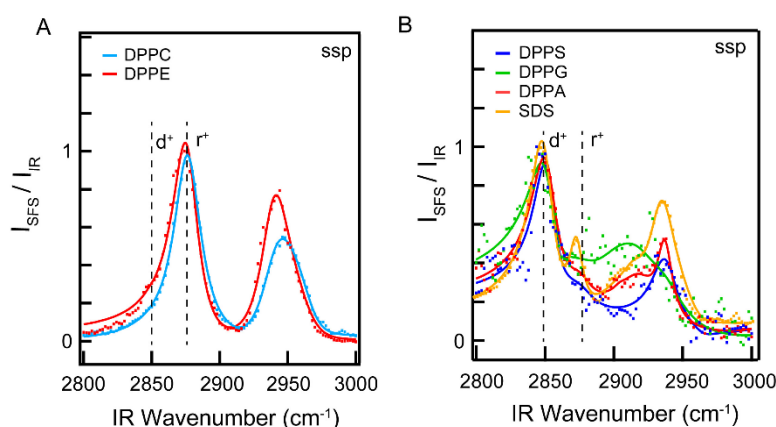

Fig. S2. The exceptional sensitivity of SFS to surface chemistry. A) Normalized SFS spectra in the C−H stretching region of 1 mM DPPC and DPPE monolayers on 100 nm radius d_{34}-hexadecane nanodroplets (2 vol %) in D_2O. The spectra are normalized to the s-CH_3 stretching mode (r^+). (B) Normalized SFS spectra of DPPS (1 mM), DPPG (1 mM), DPPA (1 mM), and SDS (10 mM) monolayers on oil (d_{34}-hexadecane) nanodroplets (2 vol %) in D_2O of the C−H stretching modes. The spectra are normalized to the s-CH_2 stretching mode (d^+). (A) and (B) are adapted from Ref. [15].

Ab initio molecular dynamics simulations

We used the software package CP2K[16], based on the Born-Oppenheimer approach, to perform ab initio molecular dynamics (AIMD) simulations of hydroxide aqueous solutions and chloride aqueous solutions under the action of static and homogeneous electric fields applied along a given direction (corresponding to the Z-axis). Similar AIMD simulations were performed for aqueous solutions containing neopentane (C_5H_{12}) in bulk water. The implementation of external electric fields in numerical codes based on Density Functional Theory (DFT) can be achieved by exploiting the Modern Theory of Polarization and Berry's phases[17-20]. Aqueous samples contained 127 H_2O molecules and one single species of hydroxide and, separately, of chloride (i.e., 383 and 382 atoms, respectively) arranged in cubic cells with side parameter equal to 15.82 Å, so as to reproduce a density of about 1 g·cm^{-3}. On the other hand, to account for an adequate solvation of neopentane, larger boxes with sides of 19.81 Å and composed of 256 water molecules and one neopentane moiety were employed for the respective simulations (i.e., 785 atoms).

Two electric field regimes were explored during the dynamics of the OH- and Cl-containing aqueous samples, namely the zero-field case and a field intensity of 10^8 V/m (0.01 V/Å). Albeit the latter value is larger than the typical electrostatic fields used in, e.g., conductivity experiments, such a strength is necessary to explore measurable diffusions of the anions in relatively short AIMD simulations while preventing known field-induced molecular dissociations[21] and vibrational Stark effects[22,23] in the samples. Similarly, a zero-field and two field regimes 0.5 x 10^9 and 10^9 V/m (i.e., 0.05 and 0.1 V/ Å) were reproduced in the neopentane AIMD simulations. Dynamics of 100 ps were afforded in the zero-field and 0.1 V/Å cases whilst a shorter trajectory of 20 ps has been produced in the intermediate case for comparison of the molecular dipole distributions. Drifts (Figure 3G of the main text and Figure S3) were determined by discarding the first half of the respective trajectories (i.e., ~50 ps) at zero field and at 0.1 V/Å. Furthermore, a series of self-consistent-field calculations without and in presence of several electric field intensities was performed both for the hydrated OH- and Cl-species both for the solvated neopentane case (see, e.g., the Hartree potential and the electronic dipole calculations in the main text, Figs. 3D and 3E).

Wavefunctions of the atomic species have been expanded in the TZVP basis set with Goedecker-Teter-Hutter (GTH) pseudopotentials using the GPW method[24]. A plane-wave cutoff of 400 Ry has been imposed. Exchange and correlation (XC) effects were treated with the gradient-corrected Becke-Lee-Yang-Parr (BLYP)[25,26] density functional. Moreover, in order to take into account dispersion interactions, we employed the dispersion-corrected version of BLYP (i.e., BLYP+D3(BJ))[27,28]. A nominal temperature slightly higher than the standard one has been simulated in order to better reproduce the water structure (i.e., T =350 K). The dynamics of ions was simulated classically within a constant number, volume, and

temperature (NVT) ensemble, using the Verlet algorithm whereas the canonical sampling has been executed by employing a canonical-sampling-through-velocity-rescaling thermostat (CSVR)[29] set with a time constant equal to 50 fs.
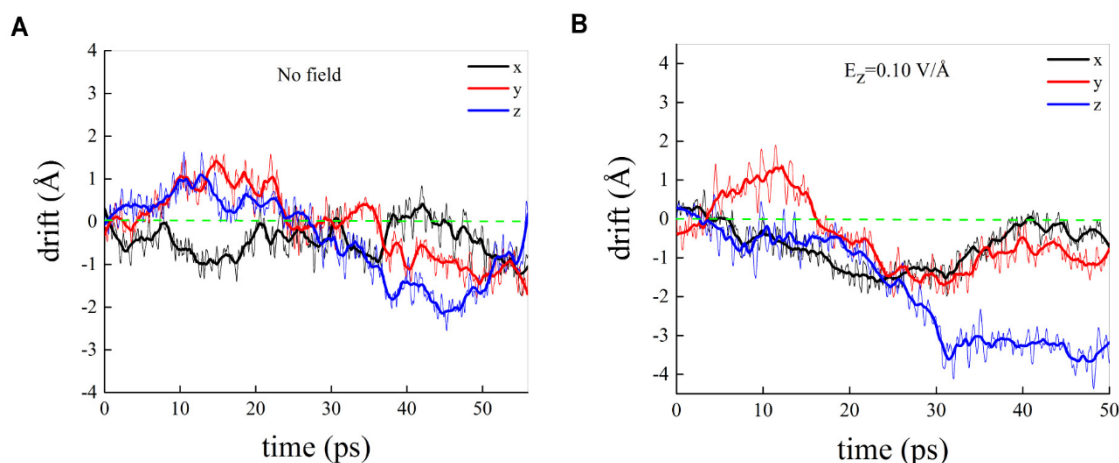

Fig. S3. Mobility of neopentane. Cartesian components of the drift of the Carbon atoms of the neopentane molecule at zero-field conditions (A) and in presence of an external static and homogeneous electric field of intensity equal to 0.1 V/Å and oriented along the z-axis (B). The net negative drift of the Cartesian component coincident with the field axis (z, blue line) magnifies the negatively charged nature of the neopentane molecule under the field action. A Savitzky-Golay smoothing (thicker lines) of the raw data (thinner lines) is also shown.

References

1   Bigelow, W. C., Pickett, D. L. & Zisman, W. A. Oleophobic monolayers: I. Films adsorbed from solution in non-polar liquids. *J. Colloid Sci.* **1**, 513-538 (1946).
2   Pullanchery, S., Kulik, S., Okur, H. I., de Aguiar, H. B. & Roke, S. On the stability and necessary electrophoretic mobility of bare oil nanodroplets in water. *J. Chem. Phys.* **152**, 241104 (2020).
3   Ohshima, H. A Simple Expression for Henry's Function for the Retardation Effect in Electrophoresis of Spherical Colloidal Particles. *J. Colloid Interface Sci.* **168**, 269-271 (1994).
4   Chen, Y. *et al.* Electrolytes induce long-range orientational order and free energy changes in the H-bond network of bulk water. *Sci. Adv.* **2**, e1501891.
5   Gonella, G., Lütgebaucks, C., de Beer, A. G. F. & Roke, S. Second Harmonic and Sum-Frequency Generation from Aqueous Interfaces Is Modulated by Interference. *J. Phys. Chem. C.* **120**, 9165-9173 (2016).
6   Lütgebaucks, C., Gonella, G. & Roke, S. Optical label-free and model-free probe of the surface potential of nanoscale and microscopic objects in aqueous solution. *Phys. Rev. B* **94**, 195410 (2016).
7   Dadap, J. I., Shan, J. & Heinz, T. F. Theory of optical second-harmonic generation from a sphere of centrosymmetric material: small-particle limit. *J. Opt. Soc. Am. B* **21**, 1328-1347 (2004).
8   de Beer, A. G. F., Campen, R. K. & Roke, S. Separating surface structure and surface charge with second-harmonic and sum-frequency scattering. *Phys. Rev. B* **82**, 235431 (2010).
9   Smolentsev, N. & Roke, S. Self-Assembly at Water Nanodroplet Interfaces Quantified with Nonlinear Light Scattering. *Langmuir* **36**, 9317-9322 (2020).

10   Levine, B. F. & Bethea, C. G. Second and third order hyperpolarizabilities of organic molecules. *J. Chem. Phys.* **63**, 2666-2682 (1975).

11   de Aguiar, H. B., Samson, J.-S. & Roke, S. Probing nanoscopic droplet interfaces in aqueous solution with vibrational sum-frequency scattering: A study of the effects of path length, droplet density and pulse energy. *Chem. Phys. Lett.* **512**, 76-80 (2011).

12   Pullanchery, S., Kulik, S., Rehl, B., Hassanali, A. & Roke, S. Charge transfer across C–H⋯O hydrogen bonds stabilizes oil droplets in water. *Science* **374**, 1366-1370 (2021).

13   Pullanchery, S., Kulik, S. & Roke, S. Water Structure at the Hydrophobic Nanodroplet Surface Revealed by Vibrational Sum Frequency Scattering Using Isotopic Dilution. *J. Phys. Chem. B.* **126**, 3186-3192 (2022).

14   Kulik, S., Pullanchery, S. & Roke, S. Vibrational Sum Frequency Scattering in Absorptive Media: A Theoretical Case Study of Nano-objects in Water. *J. Phys. Chem. C.* **124**, 23078-23085 (2020).

15   Chen, Y., Okur, H. I., Lütgebaucks, C. & Roke, S. Zwitterionic and Charged Lipids Form Remarkably Different Structures on Nanoscale Oil Droplets in Aqueous Solution. *Langmuir* **34**, 1042-1050 (2018).

16   Kühne, T. D. *et al.* CP2K: An electronic structure and molecular dynamics software package - Quickstep: Efficient and accurate electronic structure calculations. *J. Chem. Phys.* **152**, 194103 (2020).

17   Berry, M. V. Quantal phase factors accompanying adiabatic changes. *Proc. R. Soc. Lond. A* **392**, 45-57 (1984).

18   King-Smith, R. D. & Vanderbilt, D. Theory of polarization of crystalline solids. *Phys. Rev. B* **47**, 1651-1654 (1993).

19   Resta, R. Macroscopic polarization in crystalline dielectrics: the geometric phase approach. *Rev. Mod. Phys.* **66**, 899-915 (1994).

20   Umari, P. & Pasquarello, A. Ab initio Molecular Dynamics in a Finite Homogeneous Electric Field. *Phys. Rev. Lett.* **89**, 157602 (2002).

21   Cassone, G. Nuclear Quantum Effects Largely Influence Molecular Dissociation and Proton Transfer in Liquid Water under an Electric Field. *J. Phys. Chem. Lett.* **11**, 8983-8988 (2020).

22   Cassone, G., Sponer, J., Trusso, S. & Saija, F. Ab initio spectroscopy of water under electric fields. *Phys. Chem. Chem. Phys.* **21**, 21205-21212 (2019).

23   Chattopadhyay, A. & Boxer, S. G. Vibrational Stark Effect Spectroscopy. *J. Am. Chem. Soc.* **117**, 1449-1450 (1995).

24   Krack, M. Pseudopotentials for H to Kr optimized for gradient-corrected exchange-correlation functionals. *Theor. Chem. Acc.* **114**, 145-152 (2005).

25   Becke, A. D. Density-functional exchange-energy approximation with correct asymptotic behavior. *Phys Rev A* **38**, 3098-3100 (1988).

26   Lee, C., Yang, W. & Parr, R. G. Development of the Colle-Salvetti correlation-energy formula into a functional of the electron density. *Phys. Rev. B* **37**, 785-789 (1988).

27   Grimme, S., Antony, J., Ehrlich, S. & Krieg, H. A consistent and accurate ab initio parametrization of density functional dispersion correction (DFT-D) for the 94 elements H-Pu. *J. Chem. Phys.* **132**, 154104 (2010).

28   Grimme, S., Ehrlich, S. & Goerigk, L. Effect of the damping function in dispersion corrected density functional theory. *J. Comput. Chem.* **32**, 1456-1465 (2011).

29   Bussi, G., Donadio, D. & Parrinello, M. Canonical sampling through velocity rescaling. *J. Chem. Phys.* **126**, 014101 (2007).